Phase retrieval applied to stellar occultation for asteroid silhouette characterization

Russell Trahan III* and David Hyland

Department of Aerospace Engineering, Texas A&M University, HRBB 701, Ross Street,
TAMU 3141, College Station, Texas 77843, USA

*Corresponding author: rtrahan3@tamu.edu

Here we expand on the current methods of characterizing small astronomical bodies, particularly asteroids, by viewing stellar occultation events. Stellar occultation has proven to be a viable method for determining the size of moons and asteroids; however, it comes with some limitations. In general the method does not consider or use all of the known diffraction effects that occur and thus provides a nominal radius—not a shape—of the occluder. We show that most stellar occultation events involving small near-Earth asteroids occur with low Fresnel numbers. This in effect renders the traditional methods useless to characterize the shape, because no sharp shadow exists. We show that using similar data collection to that of the traditional occultation method and inverting a Fresnel diffraction equation by a phase retrieval process can yield a complete reconstruction of the silhouette of the occluder. The effect of noise in the measurements is also discussed. A practical example applied to the asteroid 25143 Itokawa is shown. © 2014 Optical Society of America

OCIS codes: (100.5070) Phase retrieval; (110.3010) Image reconstruction techniques; (350.1260) Astronomical optics; (040.1240) Arrays.

http://dx.doi.org/10.1364/AO.53.003540

1. Introduction

Stellar occultation is widely used to characterize near-Earth asteroids, minor planets, and moons, and gives reasonable estimates of the size and characteristics of some of these objects. Several successful estimates have been made of moons and Kuiper belt objects [1–3]. The method involves several observers who record the timespan in which an object occludes a specific star. Based on the position of the observers and the occultation times, the Earth ground track of the shadow can be estimated, which can then be used to estimate the size of the object. There is, however, one major limitation to this approach: it assumes that the object casts a sharp shadow. In reality the edge of a shadow is subject to diffraction; thus no clear shadow exists far away from the object. Results

such as those in [4,5] give a length estimate of an occluding object in the Kuiper belt but provide no information about the shape of the object, because they neglect some of the details of the diffraction effects. Most efforts in this field have been formulated to give a nominal radius of the occluding object, such as the discussions in [6]. The discussions in [7] expand the circular problem to include ellipses. Here the goal is to characterize the shape of an occluding asteroid with greater fidelity than a single characteristic length, radius, or geometrical shape.

As shown in Fig. 1, the effect of the occluder on the light field is based upon the distance of the observer from the object and the nominal radius of the object. The Fresnel region is the region in which a dark shadow zone exists. It is defined by the Fresnel number being greater than unity as defined by
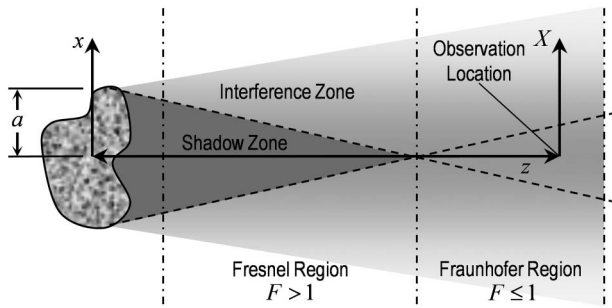
$$F = a^2/z\lambda, \tag{1}$$

Fig. 1. Schematic of an object's shadow showing the shadow zone (darkly shaded) and interference zone (lightly shaded) and the Fresnel and Fraunhofer regions. This model assumes a point source to the left of the occluder.

where a is the objects nominal radius, z is the distance of the observer from the object, and λ is the narrow-band mean wavelength of light considered [8]. A sharp shadow region only exists for $F \gg 1$. Since relatively small near-Earth asteroids are considered in this work, the Fresnel number is typically less than unity, which means no sharp shadow exists at the observer's location. Rather, only an interference pattern exists because the observer is within the Fraunhofer region. This diffraction effect is demonstrated later in an example. It is thus suggested that characterizing an object geometrically based on the shadow is not optimal. The object should be characterized by analyzing the interference pattern it produces through an intensity mapping technique, which requires a specialized method to solve the phase retrieval problem.

To formulate the problem, consider the object plane with spatial coordinates $\underline{x} = (x, y)$ and an observation plane in the Fraunhofer region with spatial coordinates $\underline{X} = (X, Y)$. Both planes are parallel and separated by the distance z, as shown in Fig. 1. The object plane can be described by the view angle from the observation location yielding $\underline{\theta} = \underline{x}/z = (\theta_x, \theta_y)$, and for convenience the observation plane coordinates can be scaled as $\underline{u} = \underline{X}/z = (u, v)$. The star far to the left in Fig. 1 is assumed to be a point source. Since the occluder is assumed to lie within the object plane, its shape defines the complex field at the object plane. The field is thus characterized by the silhouette function $\underline{\Gamma}(\underline{\theta})$, which is defined as

$$\Gamma(\underline{\theta}) = \begin{cases} 0, & \text{if } \underline{\theta} \text{ is inside the asteroid profile} \\ 1, & \text{otherwise} \end{cases}. \quad (2)$$

Propagating the field from the point source to the object plane and then to the observation plane using the Huygens–Fresnel principle applied to shadows gives the Fresnel diffraction equation [6,8–11]

$$U(\underline{u}) = \frac{z}{\lambda} \int_{\mathbb{R}^2} \Gamma(\underline{\theta}) \exp\left(\frac{i\pi z}{\lambda} \underline{\theta} \cdot \underline{\theta}\right) \exp\left(-\frac{i2\pi z}{\lambda} \underline{u} \cdot \underline{\theta}\right) d\underline{\theta}. \quad (3)$$

Notice that Eq. (3) contains the exponential term $\exp(i\pi z \underline{\theta} \cdot \underline{\theta}/\lambda)$, which introduces a periodic phase

shift into the field. The equation thus cannot be discretized and turned into a discrete Fourier transform, as is done in the traditional phase retrieval problem, unless the discretization yields elements much smaller than the wavelength of these frequencies [6]. Since often times $z/\lambda \gg 10^{10}$, such a resolution would be prohibitive computationally when considering an object plane large enough to encompass an astronomical object. Additionally, a discrete Fourier transform would not properly capture the entire object plane out to infinity. A continuous solution is thus the only apparent feasible route.

A. Problem Statement

The formal problem statement here is to devise an algorithm to estimate the shape of the occluding object's silhouette function $\Gamma(\underline{\theta})$ based on knowledge of the intensity distribution $J(\underline{u}) \equiv |U(\underline{u})|^2$. The method should be able to tolerate a reasonable level of noise in the intensity data and preferably does not require spatially high-resolution knowledge of the intensity or a priori knowledge.

B. Data Collection

Measurement of the intensity across the observation plane can be performed by multiple observers viewing the occultation event simultaneously. As has been proposed in [11] building upon [4], each observer records the time history of the observed light intensity. By comparing the intensities over small time periods within the time history, the field intensity over the observation plane can be determined. Since the Earth's motion is the dominant velocity component within the star-occluder-observer system [4], the shadow pattern moves across the observer's locations giving each observer an opportunity to measure the intensity at many locations relative to the origin of the observation plane. A schematic of the system is shown in Fig. 2, which portrays the path of the shadow pattern moving across a linear array of observers. The preliminary design places the observers on small satellites in a "string of pearls" constellation to eliminate any atmospheric effects.

2. Proposed Solution

Equation (3) is the standard Fresnel diffraction equation, which describes the wave field some distance from the occluding object; however, its
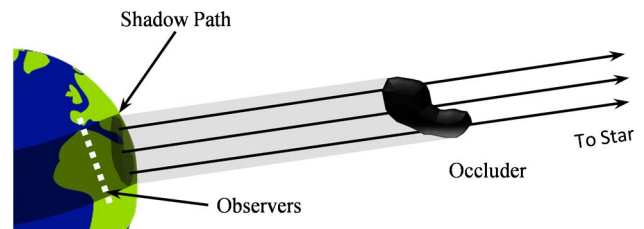

Fig. 2. Schematic of the star-occluder-observer system showing the shadow pattern moving across the Earth's surface past observers.

magnitude is the known quantity when measuring the changes in the wave field from the occluded star [11]. To simplify the expression it can be multiplied by the phase factor $\exp(i\pi z \underline{u} \cdot \underline{u}/\lambda)$, which has a magnitude of unity and is not a function of the variable of integration $\underline{\theta}$. This factor completes the square and gives the form

$$
\begin{aligned}
J(\underline{u}) &= \left| \frac{z}{\lambda} \int_{\mathbb{R}^2} \Gamma(\underline{\theta}) \exp\left(\frac{i\pi z}{\lambda} \underline{\theta} \cdot \underline{\theta} - \frac{i2\pi z}{\lambda} \underline{u} \cdot \underline{\theta} + \frac{i\pi z}{\lambda} \underline{u} \cdot \underline{u} \right) \mathrm{d}\underline{\theta} \right|^2 \\
&= \left| \frac{z}{\lambda} \int_{\mathbb{R}^2} \Gamma(\underline{\theta}) \exp\left(\frac{i\pi z}{\lambda} (\underline{u} - \underline{\theta})^2 \right) \mathrm{d}\underline{\theta} \right|^2.
\end{aligned}
\tag{4}
$$

The phase factor is benign since only the magnitude is preserved when defining $J(\underline{u})$. Equation (4) can be rewritten in the convenient form

$$
\begin{aligned}
J(\underline{u}) &= \left| \frac{z}{\lambda} \int_{\mathbb{R}^2} [1 - (1 - \Gamma(\underline{\theta}))] \exp\left(\frac{i\pi z}{\lambda} (\underline{u} - \underline{\theta})^2 \right) \mathrm{d}\underline{\theta} \right|^2 \\
&= \left| \frac{z}{\lambda} \int_{\mathbb{R}^2} \exp\left(\frac{i\pi z}{\lambda} (\underline{u} - \underline{\theta})^2 \right) \mathrm{d}\underline{\theta} \right. \\
&\quad \left. - \frac{z}{\lambda} \int_{\gamma} \exp\left(\frac{i\pi z}{\lambda} (\underline{u} - \underline{\theta})^2 \right) \mathrm{d}\underline{\theta} \right|^2,
\end{aligned}
\tag{5}
$$

where γ is the domain where $\Gamma(\underline{\theta}) = 0$. The question thus becomes how to describe the region γ such that its shape can be estimated. Since it is known that the shape of the object may not be a standard geometric shape, an obvious choice is to describe γ using a grid of binary values [12]. This would turn the second integral in Eq. (5) into a discrete summation of continuous integrals over the elements in this grid [13]. If the (i,j) element of the grid covers the domain

$$
A_{i,j} = \{(\theta_x, \theta_y) \in \mathbb{R}^2 | 0 < \theta_x - \theta_{x,i} \leq \Delta_x \wedge 0 < \theta_y - \theta_{y,j} \leq \Delta_y\}
\tag{6}
$$

and has the value $\Gamma_{i,j}$, Eq. (5) becomes

$$
\begin{aligned}
J(\underline{u}) &= \left| \frac{z}{\lambda} \int_{\mathbb{R}^2} \exp\left(\frac{i\pi z}{\lambda} (\underline{u} - \underline{\theta})^2 \right) \mathrm{d}\underline{\theta} \right. \\
&\quad \left. - \frac{z}{\lambda} \sum_{\forall i,j} (1 - \Gamma_{i,j}) \int_{A_{i,j}} \exp\left(\frac{i\pi z}{\lambda} (\underline{u} - \underline{\theta})^2 \right) \mathrm{d}\underline{\theta} \right|^2.
\end{aligned}
\tag{7}
$$

Making use of the complex form of the Fresnel integral [14]

$$
E[x] = \int_0^x \exp\left(\frac{i\pi t^2}{2} \right) \mathrm{d}t,
\tag{8}
$$

the integrals in Eq. (7) have the antiderivative

$$
\begin{aligned}
&\int_{\theta_{y,1}}^{\theta_{y,2}} \int_{\theta_{x,1}}^{\theta_{x,2}} \exp\left(\frac{i\pi z}{\lambda} (\underline{u} - \underline{\theta})^2 \right) \mathrm{d}\underline{\theta} \\
&= \left[E\left(\sqrt{\frac{2z}{\lambda}} \theta_{x,2} \right) - E\left(\sqrt{\frac{2z}{\lambda}} \theta_{x,1} \right) \right] \\
&\quad \times \left[E\left(\sqrt{\frac{2z}{\lambda}} \theta_{y,2} \right) - E\left(\sqrt{\frac{2z}{\lambda}} \theta_{y,1} \right) \right].
\end{aligned}
\tag{9}
$$

Using this expression, Eq. (7) yields [7]

$$
\begin{aligned}
J(\underline{u}) &= \left| i - \frac{1}{2} \sum_{\forall i,j} (1 - \Gamma_{i,j}) \right. \\
&\quad \times \left(E\left[\sqrt{\frac{2z}{\lambda}} (\theta_{x,i} + \Delta x - u) \right] - E\left[\sqrt{\frac{2z}{\lambda}} (\theta_{x,i} - u) \right] \right) \\
&\quad \times \left. \left(E\left[\sqrt{\frac{2z}{\lambda}} (\theta_{y,j} + \Delta y - v) \right] - E\left[\sqrt{\frac{2z}{\lambda}} (\theta_{y,j} - v) \right] \right) \right|^2.
\end{aligned}
\tag{10}
$$

The problem now is to estimate the (i,j) components of the grid, which have $\Gamma_{i,j} = 0$. This can be done by a simple guess-and-check method where the region γ is guessed, the field's squared magnitude is computed using Eq. (10), and it is compared to the measured intensity. When a suitable estimate for γ is found the two should closely match. The only difference between the two would be the fact that the true silhouette function does not follow the grid pattern that the estimation assumed [13]. The grid should thus be dense enough to mitigate this error.

An additional convenience of this method is the relaxed requirements on the intensity data resolution. The intensity data and the silhouette grid can be different resolutions. Additionally, the intensity data can be sparse since they are only used for a comparison and not a Fourier transform as is done in the traditional phase retrieval problem. The number of intensity measurements required is discussed in Section 5.

The simplest method to use for the guess and check is a raster scan across the grid. Each grid element $\Gamma_{i,j}$ is flipped in value, and the intensity distribution error is checked for improvement. The error between the estimated and measured intensity distributions can be defined by

$$
e = \sum_{\forall \underline{u}} \left| |J(\underline{\hat{u}}_{i,j})|^2 - |\hat{J}(\underline{\hat{u}}_{i,j})|^2 \right|,
\tag{11}
$$

where $\hat{u}_{i,j}$ are the locations of measurements and $\hat{J}(\underline{\hat{u}}_{i,j})$ are the measured values. If the error decreases for a change to the grid, it is kept; otherwise the value is not changed.

3. Example

To demonstrate the silhouette estimation process, consider the asteroid Itokawa as viewed from 1 astronomical unit away. The true silhouette is based on an
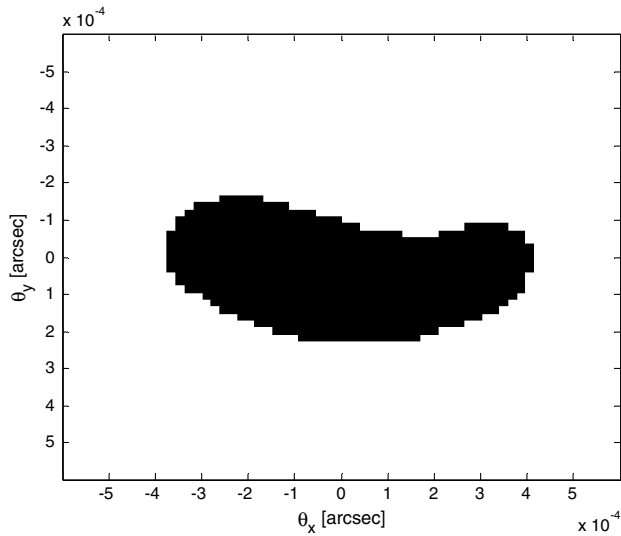
Fig. 3. True silhouette of the asteroid Itokawa pixelated in a 64×64 grid based on images from [15].

image from the Hayabusa mission and is shown in Fig. 3. The image is 64×64 pixels, and Itokawa is 40 pixels wide. Itokawa is known to be about 535 m long, so each pixel in the image is 13.4 m wide/tall. The angular resolution is thus 1.8×10^{-5} arcsec, and the field of view is 1.2×10^{-3} arcsec. This image is, therefore, unresolvable by even the Hubble telescope and is even not feasible for optical astronomical interferometers. If green light is considered, as is common in optical interferometry, the mean wavelength is 5.5×10^{-7} m. Referring to Eq. (1), the Fresnel number is thus 0.87. Since the aphelion and perihelion of Itokawa are 1.695 and 0.953 au, respectively, this example represents a reasonable case of Itokawa viewed from Earth. The intensity distribution for these parameters based upon the silhouette in Fig. 3 is shown in Fig. 4. Note the bright regions within the silhouette, which correspond to a

diffraction effect similar to the Arago spot, which reinforces the claim that the traditional occultation method of timing the disappearance and reappearance of the occluded star is unreliable [9,16].

In practice, the entire intensity map cannot be known. If the intensity is known on a grid spanning 2 km every 20 m this represents a 100×100 grid as shown in Fig. 4. It is not necessary for the measurements to follow a grid pattern. This is simply done here to make the data more convenient to display in a figure. A detailed explanation of the data collection for this application is discussed in [11] and in Section 5. It is advantageous for the measurements to span an area large enough to capture the distorted silhouette but also small enough to avoid the high frequency fluctuations that occur far away from the origin as evident in Eq. (4). Although these fluctuations are small, proper measurements far away from the origin would require tight tolerances on spatial positioning to resolve these fluctuations. Additionally, far away from the origin the field amplitude is approximately constant according to the Fresnel integral. Information far away from the origin is thus not as useful as information near the origin.

For this example the silhouette is assumed initially to be all white. The pixels in the grid are tested by flipping their values from top to bottom, left to right in a regular pattern and looking for a decrease in the error defined in Eq. (11). A complete scan across the grid is designated as one iteration. Figure 5 shows the error defined by Eq. (11) through 10 iterations. The image after just one iteration is shown in Fig. 6. The general shape of the asteroid is already apparent since the most error reduction occurs in the first iteration. Although often unnecessary for convergence, *a priori* knowledge can speed convergence. The user can manually edit the estimate before continuing to the next iteration based on intuitive knowledge that an asteroid will not typically have holes in it or any other *a priori* knowledge. This was not done for this example to prove convergence without this knowledge.

The final silhouette is shown in Fig. 7, where the input intensity matches the transformation of the estimated image, i.e., the error is nearly zero. Notice that the error drops drastically near the last
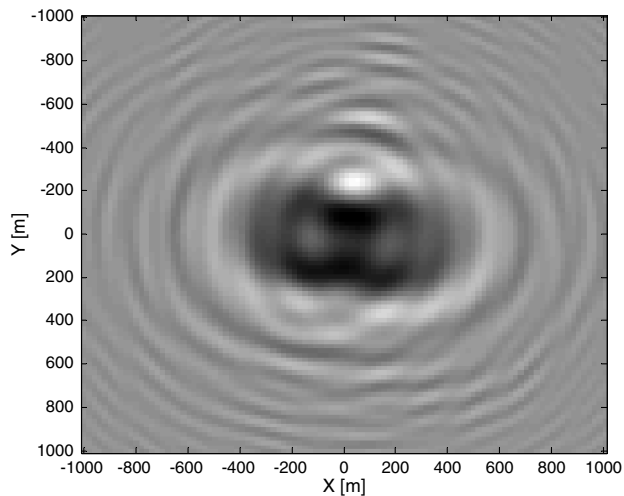

Fig. 4. Coarse grid of intensity data for the asteroid Itokawa viewed with a Fresnel number of 0.87, which serves as the input to the phase retrieval algorithm.
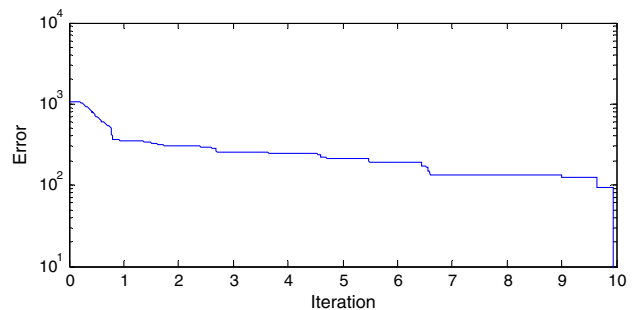

Fig. 5. Error between intensity distribution of the estimated image and the measured intensity data.
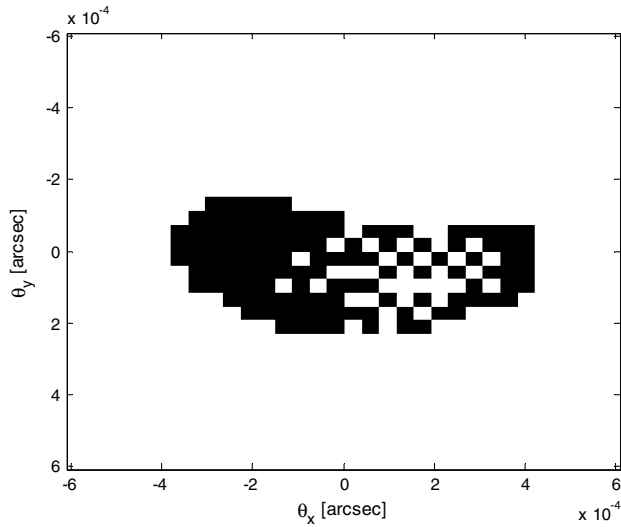
Fig. 6. Estimated silhouette of Itokawa pixelated in a 32 × 32 grid after one iteration.

iterations. This is because a single incorrect pixel accounts for the majority of the error value.

The result of the 32 × 32 image can be used as the initial estimate of a higher-resolution estimation. This has been implemented with great success. Initially a 16 × 16 or similar coarse image is computed. Its estimate serves as the input to the 32 × 32 image. This nested grid approach can reduce the number of iterations needed to recover high-resolution images and helps to ensure convergence. Using this technique the exact 64 × 64 silhouette was estimated using the 32 × 32 estimate as the initial guess in only 10 iterations.

Using the error metric in Eq. (11) has some caveats. There exist local minima in the error, which can cause the algorithm to stagnate. A convenient realization is if no error reduction takes place for an entire iteration it is known that the method
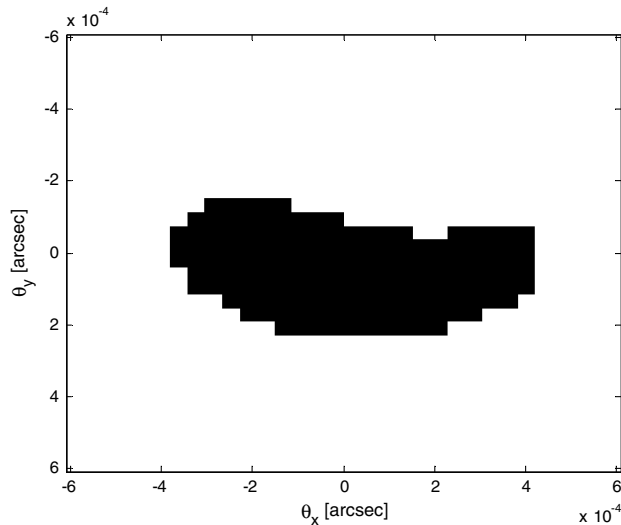

Fig. 7. Estimated silhouette of Itokawa pixelated in a 32 × 32 grid after 10 iterations.

has stagnated. A simple method to help the algorithm along is to randomly flip a few pixel values in the image. While this is a naïve approach, it often works. The optimization of this algorithm to mitigate the effect of local minima is left to subsequent work. Some ideas include testing multiple pixels at one time. Within this idea the first pixel is located using the raster scan and the second pixel is chosen at random. Since such a method introduces random behaviors, only the simplest raster scan method is shown here since the performance is deterministic.

4. Effect of Noise

The intensity measurements here are independent recordings of the field intensity. Additionally, each measurement apparatus is essentially one of the apertures of an intensity interferometer. Intensity interferometry techniques are often plagued with undesirable signal-to-noise levels; therefore, it is important that the method is capable of converging when the intensity contains random corruption. The noise model used here is commonly used in intensity interferometry and is based on the work of Hanbury Brown and Twiss [17,18]. The model is

$$\hat{J}(\underline{\hat{u}}) = |\hat{U}(\underline{\hat{u}})|^2 = |U(\underline{\hat{u}})(1 + N(0, \sigma) + iN(0, \sigma))|^2, \tag{12}$$

where $N(0, \sigma)$ is random Gaussian noise with a standard deviation of σ [19–21]. In an attempt to quantify the performance of this algorithm in the presence of noise, the 32 × 32 case for Itokawa was used in a Monte Carlo simulation. Twenty-five image estimates were constructed for different realizations of the noise at several noise levels, and no extra measures were implemented to mitigate local minima. The noise levels correspond to typical discussions of noise in phase retrieval [22,23]. The mean errors of the 25 estimates at each noise level reveal an interesting trend shown in Fig. 8. As expected, the error decreases very quickly during the first iteration. For some noise levels the error later stagnates at a nonzero level, while some converge to nearly zero.

The final error values are shown in Fig. 9. The trend that at near-zero noise levels the algorithm typically stagnates at a higher noise level than at
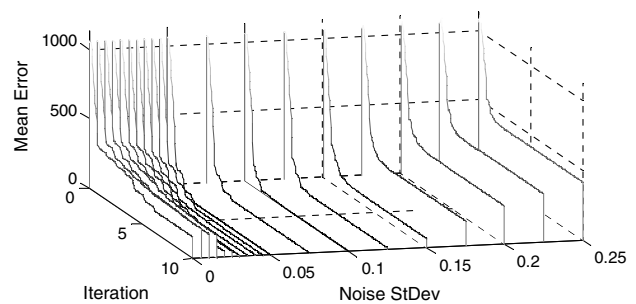

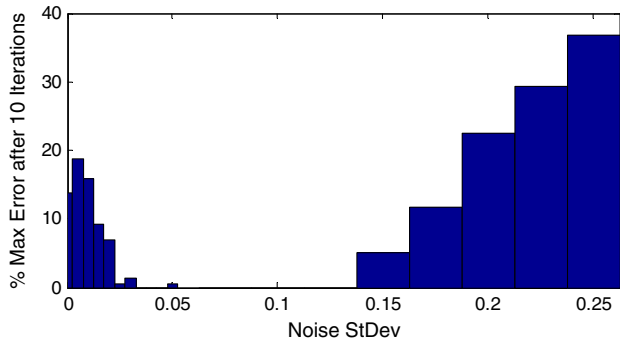Fig. 8. Monte Carlo results showing the mean error of 25 trials at several noise levels.

Fig. 9. Monte Carlo results showing the final mean error of 25 trials at several noise levels.

noise levels between 5% and 10% percent is unexpected. At near-zero noise levels the standard deviations of the Monte Carlo results are much larger than at higher noise levels. The stagnated error increases linearly above 10%. The erratic behavior for near-noiseless cases is not currently understood.

An example of the result for a noise standard deviation of 0.2 is shown in Fig. 10. The result contains some incorrect pixels, but the shape of Itokawa is clearly evident. This result can be greatly improved by a simple Gaussian image filter applied to the intensity map. The result after filtering the intensity data using a Gaussian with a standard deviation of three pixels is shown in Fig. 11. Only two pixels in the final silhouette are incorrect, and one is far enough away from the silhouette to be definitively attributed to noise. A comparable Monte Carlo simulation was performed implementing the Gaussian image filter, and the result showed no difference in the mean error near the zero noise regime; however, for higher noise levels the mean error decreased by about 25%. The result is shown in Fig. 12.
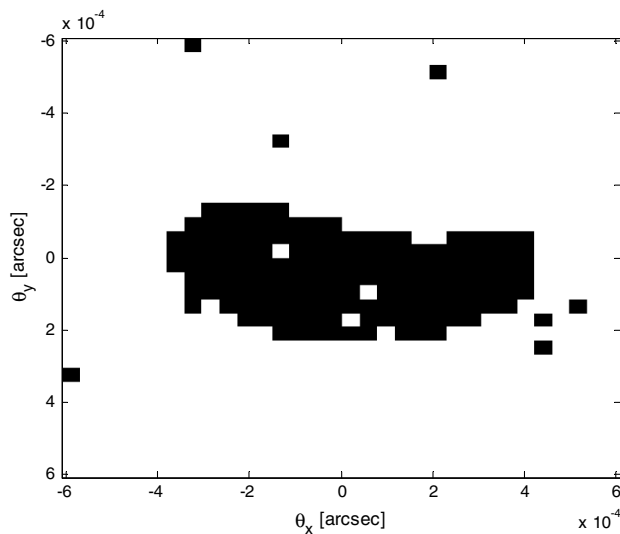

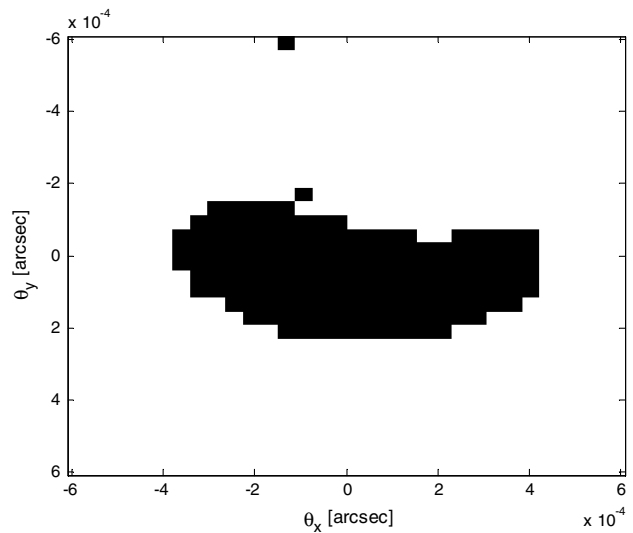Fig. 10. Example result after 10 iterations with a noise standard deviation of 0.2.

Fig. 11. Example result after three iterations with a noise standard deviation of 0.2 and a Gaussian filter applied to the intensity data.

5. Data Coverage and Aperture Positioning

The previous discussions used knowledge of the shadow pattern, which spanned a rectangular grid. In practice, the shadow pattern is only known at specified positions. Since the shadow pattern is moving at a high velocity relative to the Earth, each aperture can collect intensity measurements in a straight line across the shadow pattern. Shown in Fig. 13 is an example of the detected intensity distribution by 20 equally spaced apertures each 75 m apart with 128 measurements along each line. To quantify the quality of the data coverage the ratio of the number of measurements to the number of pixels in the silhouette estimate is defined as

$$\rho = \frac{\#\text{Measurements}}{\#\text{Pixels in Silhouette}}. \quad (13)$$

The definition of ρ can be used to establish a theoretical minimum number of measurements. The number of constraints on the system—the number of measurements—should be greater than the number
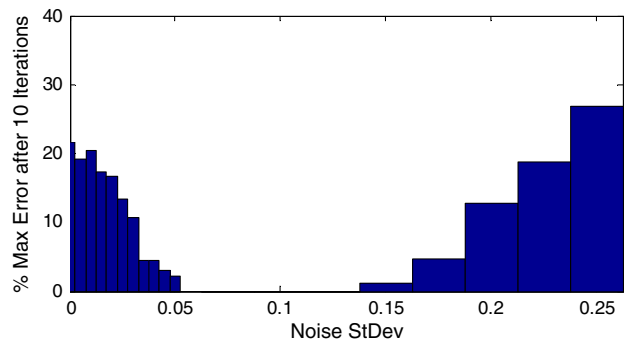

Fig. 12. Monte Carlo results showing the final mean error of 25 trials at several noise levels with a Gaussian image filter applied to the intensity data.
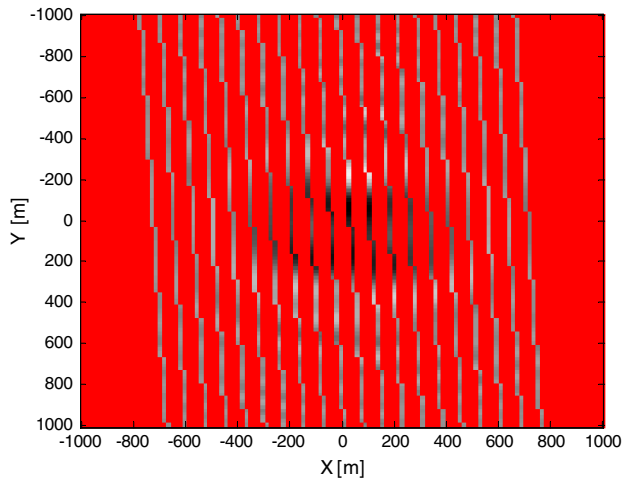
Fig. 13. Data collection pattern for 20 equally spaced apertures each 75 m apart. The red regions between the lines of data denote the absence of data. There are 128 intensity measurements along each aperture's path through the shadow pattern. The full intensity distribution is identical to Fig. 4.
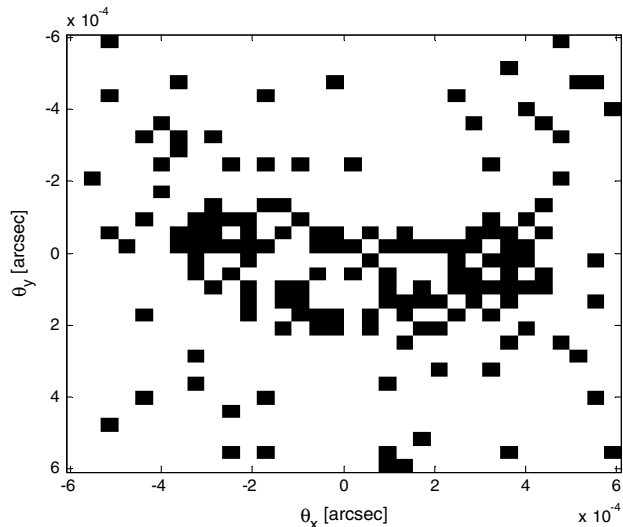

Fig. 14. Silhouette estimate for eight apertures making 128 measurements each, i.e., $\rho = 1$. This result demonstrates the need for more measurements than the theoretical minimum requirement.

of unknowns—the number of pixels in the silhouette estimate. In the case of the measurements shown in Fig. 13 used to recover a 32×32 pixel silhouette estimate, the ratio ρ is 2.5. Perfect silhouette recover was achieved after 3.6 iterations. If the number of apertures in the data collection is reduced to 8, the ratio ρ is reduced to exactly unity. In this case the recovery is theoretically possible; however, the result shown in Fig. 14 is not clear. The threshold of data collection for practical recovery requires approximately $\rho = 2$. This type of analysis can be used for testing various arrangements and spacing of the apertures. Future work on this topic will tie the silhouette estimation algorithm's performance to the design of a constellation of space borne apertures.

6. Conclusion

The discussions here take the current method of stellar occultation and expand the possible information derived from the observer data. Currently, occultation data are used to estimate a single length that corresponds to the occluder, which is based on a study of the Fraunhoffer diffraction of a circular object [9,24]. The topic of Fraunhoffer diffraction of noncircular objects has been explored but not with the practical application discussed here [25,26]. Here the same type of light collector is used for data collection; however, the information is processed differently to yield a complete silhouette of the occluder of much higher resolution than any of the light collectors can individually resolve.

It has been shown previously that the diffraction pattern produced by an occluder can be considered a convolution of the pattern produced by the occluder split into simpler geometric shapes [7]. Here this idea was expanded and formalized yielding an expression for the diffraction pattern of an arbitrary occluder. An algorithm was presented that is capable of inverting the formula for the diffraction pattern, which yields the shape of the occluder for a given diffraction pattern's intensity distribution. Examples of the algorithm's performance were shown using the silhouette of Itokawa. The resolution and dimensions in the example represent Itokawa viewed from one astronomical unit away. The algorithm was able to reconstruct the silhouette at various resolutions. The algorithm was also tested in the presence of various levels of noise. The simple method of smoothing the intensity data with a Gaussian filter reveals a measurable improvement in the resulting image quality. Additionally, the performance of the algorithm was shown for a practical number of apertures in a defined constellation.

Ongoing work on this topic includes optimizing the silhouette recovery algorithm to decrease runtimes for high-resolution images and escape local minima of the error metric. Additionally, the analysis is being expanded to assume a finite disk for the star instead of a point and a finite bandwidth instead of the small bandwidth assumption. A better performing method of noise filtering in the intensity data is also sought. Future work will also focus on the development of the aperture constellation.

References

1. J. L. Elliot, M. J. Person, C. A. Zuluaga, A. S. Bosh, E. R. Adams, T. C. Brothers, A. A. S. Gulbis, S. E. Levine, M. Lockhart, A. M. Zangari, B. A. Babcock, K. DuPré, J. M. Pasachoff, S. P. Souza, W. Rosing, N. Secrest, L. Bright, E. W. Dunham, S. S. Sheppard, M. Kakkala, T. Tilleman, B. Berger, J. W. Briggs, G. Jacobson, P. Valleli, B. Volz, S. Rapoport, R. Hart, M. Brucker, R. Michel, A. Mattingly, L. Zambrano-Marin, A. W. Meyer, J. Wolf, E. V. Ryan, W. H. Ryan, K. Morzinsky, B. Grigsby, J. Brimacombe, D. Ragozzine, H. G. Montano, and A. Gilmore, "Size and albedo of Kuiper belt

object 55636 from a stellar occultation," Nature **465**, 897–900 (2010).

2. B. Sicardy, A. Bellucci, E. Gendron, F. Lacombe, S. Lacour, J. Lecacheux, E. Lellouch, S. Renner, S. Pau, F. Roques, T. Widemann, F. Colas, F. Vachier, R. Vieira Martins, N. Ageorges, O. Hainaut, O. Marco, W. Beisker, E. Hummel, C. Feinstein, H. Levato, A. Maury, E. Frappa, B. Gaillard, M. Lavayssiere, M. Di Sora, F. Mallia, G. Masi, R. Behrend, F. Carrier, O. Mousis, P. Rousselot, A. Alvarez-Candal, D. Lazzaro, C. Veiga, A. H. Andrei, M. Assafin, D. N. da Silva Neto, C. Jacques, E. Pimentel, D. Weaver, J.-F. Lecampion, F. Doncel, T. Momiyama, and G. Tancredi, "Charon's size and an upper limit on its atmosphere from a stellar occultation," Nature **439**, 52–54 (2006).

3. B. Sicardy, A. Brahic, C. Ferrari, D. Gautier, J. Lecacheux, E. Lellouch, F. Roques, J. E. Arlot, F. C. Colas, W. Thuillot, F. Sevre, J. L. Vidal, C. Blanco, S. Cristaldi, C. Buil, A. Klotz, and E. Thouvenot, "Probing Titan's atmosphere by stellar occultation," Nature **343**, 350–353 (1990).

4. H. E. Schlichting, E. O. Ofek, M. Wenz, R. Sari, A. Gal-Yam, M. Livio, E. Nelan, and S. Zucker, "A single sub-kilometre Kuiper belt object from a stellar occultation in archival data," Nature **462**, 895–897 (2009).

5. F. Rogues, A. Doressoundiram, V. Dhillon, T. Marsh, S. Bickerton, J. J. Kavelaars, M. Moncuquet, M. Auvergne, I. Belskaya, M. Chevreton, F. Colas, A. Fernandez, A. Fitzsimmons, J. Lecacheux, O. Mousis, S. Pau, N. Peixinho, and G. P. Tozzi, "Exploration of the Kuiper Belt by high-precision photometric stellar occultations: first results," Astron. J. **132**, 819–822 (2006).

6. E. F. Young, "A Fourier optics method for calculating stellar occultation light curves by objects with thin atmospheres," Astron. J. **749**, 1–13 (2012).

7. F. Roques, M. Moncuquet, and B. Sicardy, "Stellar occultations by small bodies: diffraction effects," Astron. J. **93**, 1549–1558 (1987).

8. O. K. Ersoy, *Diffraction, Fourier Optics and Imaging* (Wiley-Interscience, 2007).

9. R. E. English and N. George, "Diffraction patterns in the shadows of disks and obstacles," Appl. Opt. **27**, 1581–1587 (1988).

10. M. Born and E. Wolf, *Principles of Optics*, 6th ed. (Cambridge University, 1997).

11. D. Paganin, *Coherent X-Ray Optics* (Oxford University, 2006).

12. J. Komrska, "Simple derivation of formulas for Fraunhofer diffraction at polygonal apertures," J. Opt. Soc. Am. **72**, 1382–1384 (1982).

13. H. Altwaijry and D. Hyland, "Detection and characterization of near Earth asteroids using stellar occultation," in *AAS/AIAA Astrodynamics Specialist Conference*, Hilton Head, South Carolina (2013), pp. 13–942.

14. V. Laude, "Diffraction analysis of pixelated incoherent shadow casting," Opt. Commun. **138**, 394–402 (1997).

15. F. L. Pedrotti, L. M. Pedrotti, and L. S. Pedrotti, *Introduction to Optics*, 3rd ed. (Pearson, 2014).

16. M. Abramowitz and I. A. Stegun, "Error function and Fresnel integrals," in *Handbook of Mathematical Functions* (Dover, 1972), pp. 300–302.

17. "JAXA," [Online]. Available: http://www.isas.jaxa.jp/j/snews/2005/1101_hayabusa.shtml. [Accessed 2014].

18. R. H. Brown and R. Q. Twiss, "A new type of interferometer for use in radio astronomy," Nature **178**, 1046–1048 (1956).

19. R. H. Brown, "Stellar interferometer at Narrabri Observatory," Nature **218**, 637–641 (1968).

20. D. Dravins, S. LeBohec, H. Jensen, and P. Nunez, "Optical intensity interferometry with the Cherenkov Telescope Array," Astroparticle Phys. **43**, 331–347 (2013).

21. R. H. Brown and R. Q. Twiss, "The question of correlation between photons in coherent light rays," Nature **178**, 1447–1448 (1956).

22. R. Trahan and D. Hyland, "Mitigating the effect of noise in the hybrid input-output method of phase retrieval," Appl. Opt. **52**, 3031–3037 (2013).

23. J. R. Fienup and C. C. Wackerman, "Phase-retrieval stagnation problems and solutions," J. Opt. Soc. Am. A **3**, 1897–1907 (1986).

24. G. Liu, "Object reconstruction from noisy holograms: multiplicative noise model," Opt. Commun. **79**, 402–406 (1990).

25. L. J. Palumbo and A. M. Platzeck, "Diffraction by a circular aperture: a new approach," J. Opt. Soc. Am. A **4**, 839–842 (1987).

26. A. Borovol, E. Naats, U. Oppel, and I. Grishin, "Shape characterization of a large nonspherical particle by use of its Fraunhofer diffraction pattern," Appl. Opt. **39**, 1989–1997 (2000).